

Chapter 5

Nonlinear Focused Beams by Axisymmetric Gratings

Abstract

Previously, we presented the diffraction of waves on axisymmetric uniform gratings can conform a Bessel beam. Here, the spacing between slits is designed in order to provide focusing as in Fresnel Zone Plates. The device presents a very narrow focal spot, that is between the sub-diffraction and the sub-wavelength limits. As common from other Fresnel-like lenses, and also in Bessel beams, the narrow focal is accompanied by high amplitude side lobes. The lens presents high gain, around 30 dB. Thus, nonlinear effects can mainly activated locally at the focal spot. The field of the second harmonic maintain the excellent beam-width of the Fresnel lens, while its side-lobes are strongly reduced. The proposed lens in the weakly nonlinear regime is suitable for second harmonic imaging techniques: the excellent beam spatial resolution of the second harmonic is maintained, while the side-lobe amplitude, responsible of signal-to-noise ratio, is reduced.

5.1 Introduction

Acoustic focusing is an interdisciplinary topic covering a rich set of applied sciences that include nondestructive testing and acoustic microscopy techniques, detection of fish and undersea exploration, ultrasound and elasticity diagnostic imaging or ultrasound therapeutic techniques among others. Particularly interesting is the fact that focusing results in high intensities at a specific location and over only a small volume, triggering nonlinear acoustics effects and enhancing specific mechanical and thermal effects. Mechanical phenomena include cavitation, microstreaming, and acoustic radiation forces while the thermal effects include heat generation due to acoustic energy absorption.

These nonlinear effects are exploited by a broad range of applications. In ultrasound medical applications second harmonic generation is widely used in harmonic imaging techniques as in Tissue Harmonic Imaging (THI) (Averkiou et al., 1997), microbubble cavitation processes are commonly used for increase contrast in ultrasound imaging (Duck, 2002), to induce mechanical interaction with the surrounding tissues in ultrasound-enhanced drug delivery techniques (Bailey et al., 2003) or for noninvasive blood-brain barrier opening using focused ultrasound (Choi et al., 2007). Acoustic radiation forces are exploited to map media elasticity in ultrasound elastography techniques such as in Shear Wave Elasticity Imaging (SWEI) (Sarvazyan et al., 1998), Acoustic Radiation Force Impulse imaging (ARFI) (Nightingale et al., 2002), Harmonic Motion Imaging (HMI) (Konofagou et al., 2003) or in Supersonic Shear Imaging (SSI) (Bercoff et al., 2004). Moreover, at high intensities nonlinearity increase energy deposition rate, that is exploited in High Intensity Focused Ultrasound (HIFU) for enhancing thermal ablation (Bailey et al., 2003). Finally, in the case of Shock Wave Lithotripsy (SWL) acoustic pulsed-shock waves are focused to produce high-amplitude localized shear stresses and induce calculus fragmentation, as widely used for kidney stone treatments (Bailey et al., 2003). In all of these techniques, the design of devices to easily manage the focusing properties and the enhancement of the focal gain is of pivotal importance.

Acoustic focusing can be achieved by arrays of transducers where the beam focusing and steering can be controlled actively, where its focusing performance is limited by the number of active channels. It is attractive the design of passive acoustic focusing devices in order to reduce costs.

Generally, there are four main different procedures to generate strongly focused acoustic field by passive devices: by optimizing the geometry of the transducer, by using refraction lenses, by using reflective systems or by using diffraction gratings. The most common approach is to use curved shaped radiation surfaces. These can be made by curved bowl single element piezoelectric transducers, but also from different arrangements of small plane transducers distributed over a curved surface and excited in-phase. Curved acoustic lenses made of different refraction

index material are also common, as long the lens is also used as an impedance matching layer between the active element, and the surrounding media. However, the transmission efficiency of these lenses is strongly reduced because the contrast of refraction index between the lens and the surrounding media is remarkable. On the other hand, focusing can be achieved by curved reflectors, e.g. elliptic reflectors in SWL. Due to the low dispersion of the acoustic media, all these focusing devices based on refraction, and also based on reflection of curved surfaces, present the feature that focusing does not strongly depends on frequency and therefore are suitable for impulsive excitations. However, in these devices, in which the focal sport is limited by the diffraction limit (Rayleigh criterion), the focal size is larger than one wavelength, i.e. the focal resolution is bigger than the sub-wavelength regime.

The last group of passive devices to generate strongly ultrasound focusing is based on the diffraction grating. The diffraction of waves on flat grating plates have been proposed as acoustic analogues of the Fresnel Zone Plates (FZP) (Farnow et al., 1974; Sleva et al., 1994; Schindel et al., 1997; Wang et al., 2008). As in optics, acoustic Fresnel Zone Plates consist of alternating rigid (opaque) and open (transparent) annuli. The radius and width of the open annuli are specially designed to only transmit the waves that constructively interferes at focus, while the radiation that destructively interferes is blocked by the rigid annuli. There exist other approaches that exploit the diffraction over concentric ringed-shaped structures to achieve focalization. These include axisymmetric gratings based on Fresnel Zone Plates in which the area of the annuli is not equal for opaque and transparent zones (Clement et al., 2015) or acoustic Fresnel lenses that exploit resonances to enhance the transmission (Molerón et al., 2014).

It is worth noting here that the diffraction grating over equally spaced toroidal scatters, as those presented in Chapter 4, can generate Bessel beams at the axis (Jimenez et al., 2014). This approach is roughly equivalent to the Bessel beams created by annular piezoelectric annuli (Hsu et al., 1989b). A characteristic feature of Bessel beams is that the transverse beam-width can be reduced below the sub-wavelength limit. However, these beams present also high amplitude side-lobes. Thus, when used for imaging, these devices provides high spatial resolution but low signal-to-noise (S/N) ratios (Lu et al., 1990b).

As soon as high amplitudes are applied to these focusing devices, it is well-known that the second harmonic field is generated mainly around the focal spot due to the local activation of the nonlinear response of the media. The focus of the second harmonic has reduced side-lobes as long the nonlinear processes are mainly activated at the focal spot (Duck, 2002). In the case of ideal Bessel beams, it has been observed a reduction of half intensity of the side-lobe amplitude for the second harmonic component (Ding et al., 1996), while its transverse profile is reduced to the half, i.e. exactly maintain its narrowness if normalized to the wavelength (Ding et al., 2000b). These effects have been also observed in more realistic configurations including absorption (Cunningham et al., 2000b) and limited

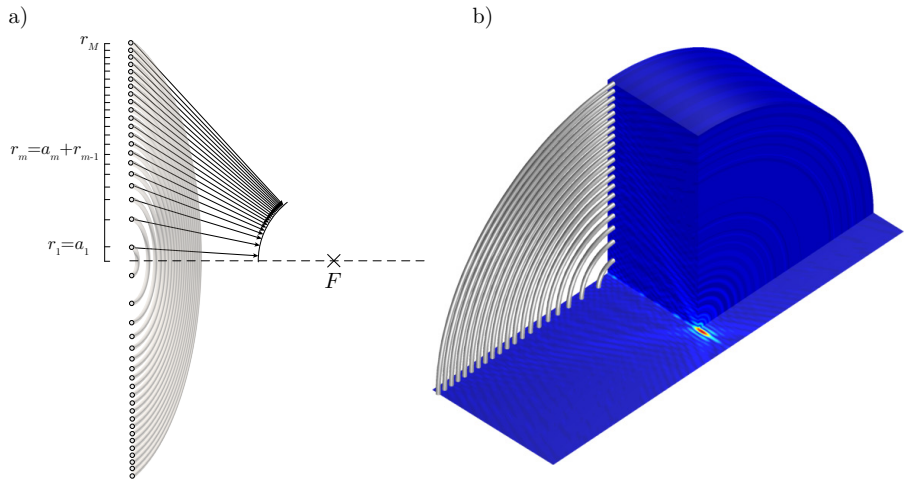


Figure 5.1: (a) Scheme of the passive focusing device composed of concentric rings. (b) Simulation example of focusing by this device.

aperture Bessel beams (Holm et al., 2010). Recently, the reduction of side-lobes of second harmonic has been observed for a focused Fresnel field, where the focalization, instead of passive lenses, has been achieved by active Fresnel beamforming in the context of second harmonic imaging (Nguyen et al., 2014).

In this Chapter, we present the acoustical focusing properties of an axisymmetric diffraction grating in both the linear and the nonlinear regime. We show that in the linear regime the system presents a focal spot in the sub-wavelength regime with high gain, around 30 dB, with relative high amplitude side-lobes. Interestingly, nonlinear effects can be excited locally mainly at the sharp focal spot. Thus, in the nonlinear regime the high intensity at the focal spot activates the harmonic generation, producing a focus of the second harmonic with particular spatial features. Mainly, second harmonic beam-width is between sub-diffraction and sub-wavelength limits, but having strongly reduced lateral lobes.

We demonstrate these results by analytical estimations, numerical simulations and experiments. A simple analytical model based on an approach of axisymmetric diffraction gratings is used to estimate the focal positions and the extent of the focal spot. Numerical calculations (using finite-difference time domain (FDTD) techniques (Botteldooren, 1995)) of acoustic waves propagating through such axisymmetric gratings were used to observe the complete acoustic field in both the linear and the nonlinear regime. The experimental verification of the theoretical prediction is also reported showing very good agreement with the theory.

5.2 Axisymmetric diffraction grating design

We consider M concentric toroidal scatterers of minor radius R and major radius r_m with $m = 1, ..., M$. A detailed scheme is presented in Fig. 5.1 (a). A plane wave radiates the axisymmetric grating and as a consequence it is scattered. We consider that R is small in comparison to the wavelength of the incident wave, in such a way that each scatterer can be considered as a point source. Then, in order to have an optimal superposition at a given focal point, F, behind the axisymmetric grating, all the incoming waves should arrive precisely in phase to F. This suggests an ideal axisymmetric grating would consist of a series of infinitesimal toroidal scatterers located in a plane at radial distances given by the geometric focal law

$$r_{m+1}^2 = r_m^2 + n\lambda\left(n\lambda + 2\sqrt{r_m^2 + F^2}\right), \tag{5.1}$$

where n indicates the diffraction order of the axisymmetric diffraction grating. Equivalently, given the distribution of toroidal scatterers, r_m, the focal position can be determined by the following expression,

$$F = \sqrt{\left(\frac{r_{m+1}^2 - r_m^2}{2n\lambda} - \frac{n\lambda}{2}\right)^2 - r_m^2}. \tag{5.2}$$

Here, it is important to note the relation of Eq. (5.1) to the standard Fresnel Zone Plate. As explained above, FZP consist in alternating opaque and open annuli. The location of the edges for the m zone is given by

$$r'_m = \sqrt{\left(\sqrt{r_0 + F^2} + m\frac{\lambda}{2}\right)^2 - F^2}. \tag{5.3}$$

The location of the center of each annuli in the standard FZP is given by (Clement et al., 2015)

$$r_m = \sqrt{\left(\sqrt{r_0 + F^2} + m\lambda\right)^2 - F^2}, \tag{5.4}$$

which gives same radial distribution of the toroidal rings as the succession obtained by diffraction grating in Eq. (5.1) if the proper first toroidal radius is matched for both lenses. On the other hand, in the work of Clement et al. (2015) they study a lens formed by slits of different thickness located at r_m, while in the present work we used rigid scattered located at r_m. Following Babinet's principle considerations, both approach can be considered equivalent.

Figure 5.1 (b) presents a simulation example of the focalization. As long the separation between the external rings is about one wavelength, it can be seen qualitatively the focusing of the system, the focal spot and the good spatial resolution

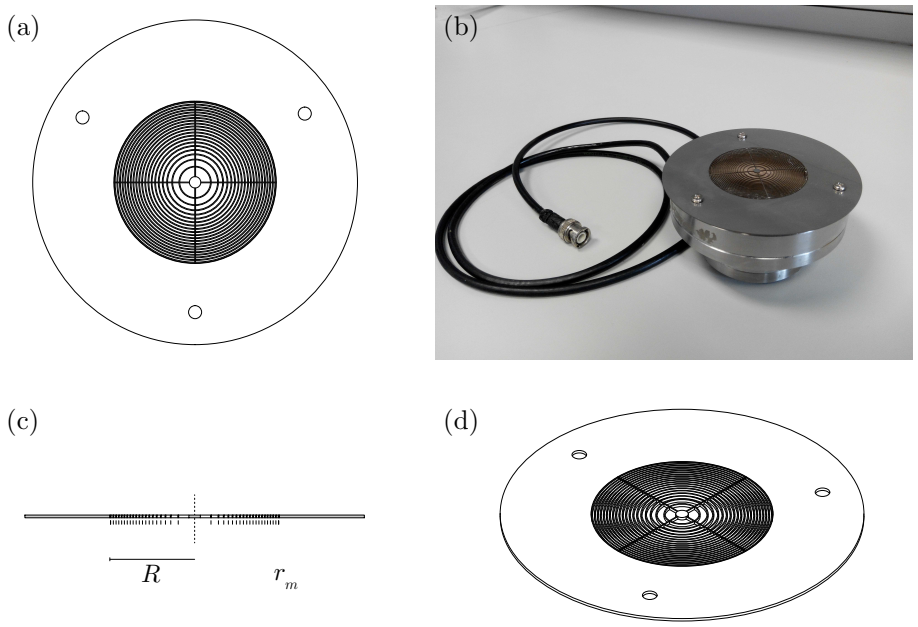


Figure 5.2: (a,c,d) Design of the axisymmetric grating plate. (b) Image of the constructed grating mounted over a plane piezoelectric transducer of 50 mm aperture.

compared to the wavelength. In the following sections a further analysis of the focusing quality of this design is presented.

5.3 Small amplitude focusing

An experiential test was performed in order to validate model results. Following the design Eq. (5.1), an axisymmetric grating was designed by using a focal distance of $F = 15$ mm and focal frequency $f_0 = 2.29$ MHz. The passive system was fabricated by laser cutting over a stainless steel plate of 0.8 mm thickness. Figures 5.2 (a,c,d) show a scheme of the axisymmetric grating. The minor radius of the toroidal scatterers was $R = 0.75$ mm (solid parts). The number of rings was $M = 21$ and the grating total radius was $r_M = 25$ mm.

The axisymmetric grating lens was placed in front of an ultrasound plane transducer as shown in Fig. 5.2 (b). This source was formed by a plane single element piezoceramic crystal (PZ 26, Ferroperm Piezoceramics, Denmark) mounted in a custom designed steel housing with aperture $R = 25$ mm, matching the area of the grating. The separation distance between the grating and the source plane was adjusted to 0.5 mm.

The assembled grating-transducer system was immersed in a degassed and distilled water tank of $350 \times 350 \times 350$ mm^3, the temperature of which during the measurements was constant at 26 °C. The source was driven with a sinusoidal sweep burst ranging from frequency $f_{\min} = 1$ MHz to $f_{\max} = 3$ MHz and 50 cycles using a function generator (14 bits, 100 MS/s, model PXI5412, National Instruments) and a linear RF amplifier (ENI 1040L, 400W, 55dB, ENI, Rochester, NY). The pressure waveforms were acquired with a HNR 500 μm needle PVDF hydrophone (Onda Corp, CA), and a digitizer (64 MS/s, model PXI5620, National Instruments) were used. A three-axis micropositioning system (OWIS GmbH, Germany) was used to move the hydrophone in three orthogonal directions with an accuracy of 10 μm and a National Instruments PXI-Technology controller NI8176 was used to control all the devices. The amplitude frequency response of the hydrophone was compensated in post-processing.

In addition to measurements, we perform numerical simulations in order to explore the linear character of the designed axisymmetric diffraction grating. For the numerical simulations we calculate the wave propagation using the FDTD technique considering an incident plane wave of unity amplitude, $p_0 = 1$ Pa. From

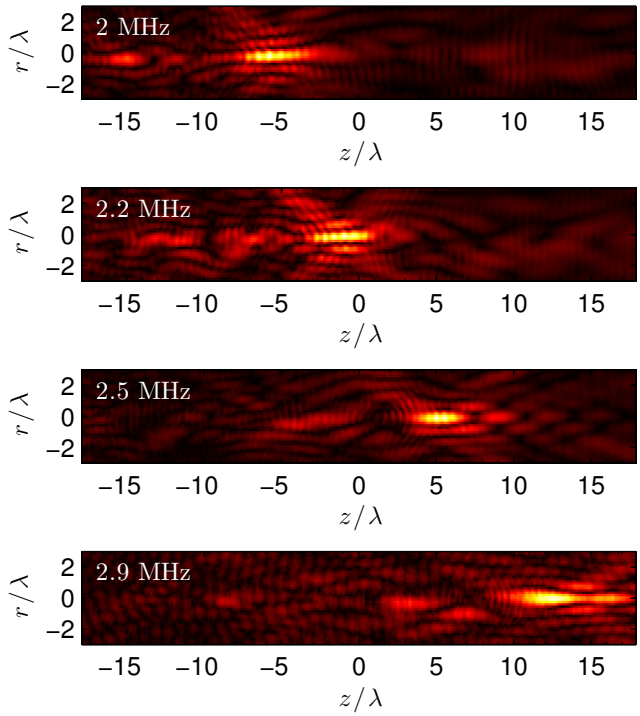


Figure 5.3: Field distribution for four different frequencies obtained by the experiment. It can be seen how the focal spot displaces in the axial location.

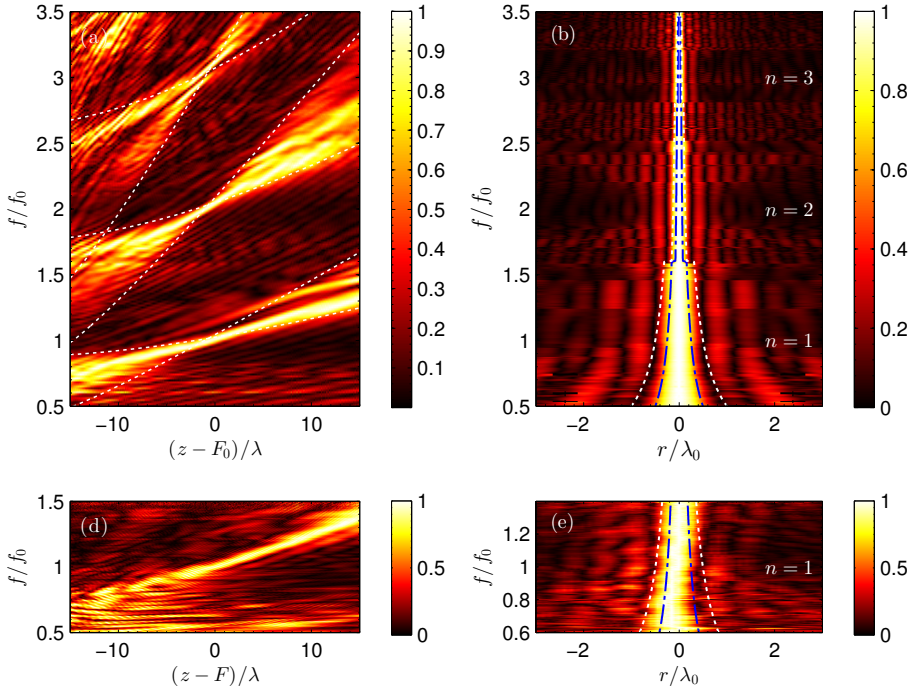


Figure 5.4: On axis field distribution as a function of frequency obtained by (a) simulation and (c) experiment. White lines indicates theoretical focus by using Eq. (5.2). Transverse field distribution measured at the focal spot axial distance as a function of frequency obtained by (b) simulations and (d) experiment. White lines mark the sub-wavelength and blue lines the sub-diffractive limit.

now we will show the results in normalized units. Distances will be normalized with respect to the wavelength, λ, and in the case of the distances in the symmetry axis will be referred to the focal distance F; frequencies will be normalized to the design frequency, f_0.

Figure 5.3 shows the experimental pressure distribution for different frequencies around the design frequency $f_0 = 2.229$ MHz. It can be seen that a sharp focusing is observed for the design frequency. Furthermore, if frequency is modified the focal position displaces in the axial direction according to Eq. (5.2). In these cases, some focus aberration appears as long the design model holds exact only for the design frequency (Fig. 5.3 (b)). However, the focal spot maintains its shape and focusing properties for a reasonably bandwidth that we will study in the following sections.

The axial pressure distribution as a function of frequency is presented in Fig. 5.4 (a) for the simulations and Fig. 5.4 (c) for the experiment. Note that, due to the finite bandwidth of the ultrasonic source, in the experimental measurements

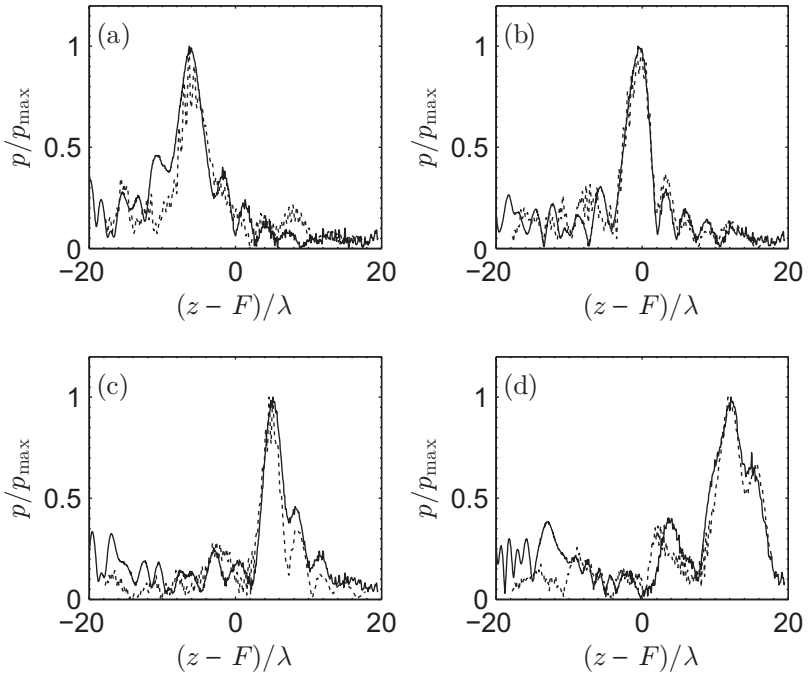


Figure 5.5: (a-d) On-axis pressure measured for the frequencies $f = 2, 2.2, 2.5, 2.9$ MHz respectively obtained by (doted lines) experiments and (continuous lines) simulations.

the characterization is restricted to a frequency range covering the first diffraction grating mode, i.e., $n = 1$, while in the simulations the characterization is extended for frequencies covering up to $n = 3$ diffraction orders. White dotted line represents the curves obtained from Eq. (5.2) for two different pairs of m, ($m = 1$ and $m = 21$), the crossing of this line represents the focal point. The agreement with the numerical simulation is very good. Moreover, one can see that although the lens is designed to focus waves in the point F at frequency f_0, the lens produces a focal shift with frequency giving the possibility to manage the position of the focus with frequency. However, as we will see later, the gain at focal spot changes considerably with frequency. Finally, we notice that as we increase frequency in the simulations new focal spots are generated for the higher diffraction grating orders. according to Eq. (5.2).

Figures 5.4 (b, d) represents the radial distribution of the normalized acoustic field at the position of the focal spot: Fig. 5.4 (b) shows the simulation while Fig. 5.4 (d) shows experimental results. Figures 5.4 (a, c) represents the equivalent radial distribution to the results of Figs. 5.4 (b, d) respectively. We can observe a main lobe aligned with the center of the axisymmetric lens. Secondary smaller lobes also appears. We also represent the the theoretical Full Width at Half Maximum (FWHM) corresponding to (dotted white lines) sub-wavelength ($< \lambda$) and

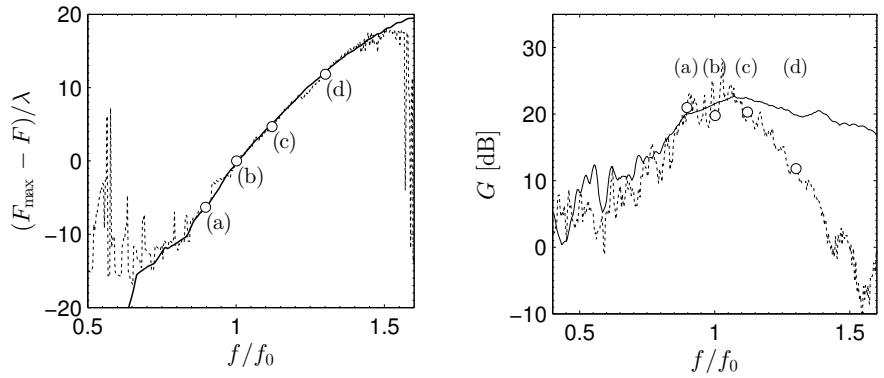


Figure 5.6: (Left) Location of the focal obtained by (dotted lines) experiments and (continuous line) simulations. (Right) Gain value obtained by (dotted lines) experiments and (continuous line) simulations. Markers (a-d) corresponds to the frequencies $f = 2, 2.22.5, 2.9$ MHz respectively.

(dashed blue lines) subdiffractive ($< \lambda/2$) limits respectively. At first glance, we can observe that in both, simulations and experiments, the width of the focal spot between the sub-diffractive and sub-wavelength regime, overcoming the diffraction limit. A deeper analysis is presenter later.

In order to see the agreement between experiments and theory, we have plotted in Fig. 5.5 the longitudinal cuts of the normalized acoustic pressure for the cases $f = 2, 2.2, 2.5, 2.9$ MHz, in the subplots (a-c) respectively. Continuous line represents the numerical predictions while dashed lines show the experimental results. Good agreement is seen in all cases, where again it can be seen how the focal spot is shifted in axial direction for increasing frequencies. The shifting of the focal position can be seen in detail in Fig. 5.6 (left), where it is represented the location of the peak pressure for the (continuous line) simulations and (dashed lines) experiment. Excellent agreement is observed between them. The frequencies corresponding to $f = 2, 2.2, 2.5, 2.9$ MHz, are marked as the points (a-c).

In order to evaluate the focusing capability of the axisymmetric grating we are discussing in this work, we have analyzed the gain of the lens evaluating the expression $G = 20 \log (|p_{\max}|/|p_0|)$ [dB], where $p_{\max}$ is the pressure at the focal point and $|p_0|$ is the incident wave pressure amplitude. Figure 5.6 (right) shows the gain numerically evaluated (continuous line) and experimentally measured (dotted line). For the design of this lens with $M = 21$ scatterers, the gain is 20 dB. We notice that this gain is constant around $f/f_0 = 1$, so the focusing properties of the axisymmetric lens is robust in terms of frequency, i.e., it is insensitive to possible errors in frequency around $f/f_0 = 1$.

Figure 5.7 (left) goes further and shows a general overview of the gain of a lens designed with the Eq. (5.1) as the number of toroidal scatterers, M is increased.

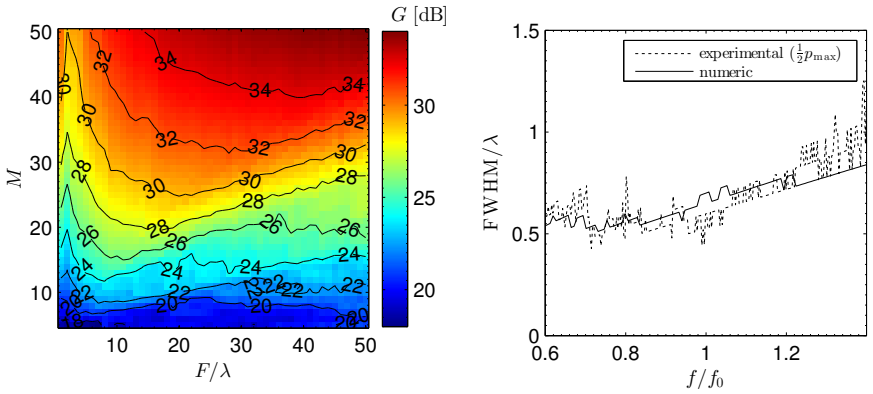


Figure 5.7: (Left) Simulated gain value measured at the design frequency for different gratings, as a function of the number of rings, M, and the design focal distance, F. (Right) Full Width at Half Maximum (FWHM) obtained by (dotted lines) experiments and (continuous line) simulations, measured at the half pressure.

By using double number of toroidal scatterers, $M = 42$, the gain of the system can be increased to 34 dB. We notice that this amount of gains are competitive with the usual systems used in high intensity focused ultrasound (Canney et al., 2008), but note we can achieve these values for very short distances. It is worth noting here that we can achieve these high gains at very short focal distances, of the order of wavelength. This property is almost impossible with with other common passive devices due to geometrical limitations. A further discussion is reported in the Conclusions section.

Finally, we have analyzed the Full Width at Half Maximum (FWHM) of the radial dimensions of the focal spot in the whole range of frequencies. Figure 5.7 (right) shows the (continuous line) numerical predictions and the (dotted line) experimental results for the FWHM. The axisymmetric lens presented in this work, shows a sub-wavelength full width at half maximum, i.e., FWHM $< \lambda$, for the whole range of analyzed frequencies. We also calculated the FWHM evaluated from the intensity data, i.e. the with of the spot at $p = p_{\max}/\sqrt{2}$. Obviously the width of the focal evaluated by intensity is thinner but the same concussions applies here: the central radial lobe corresponding to the focal spot is always between the sub-wavelength regime and the diffraction limit. This feature can be also observed by the white dashed lines in the maps shown in Figs. 5.4 (b, d).

5.4 Transition from linear-to-nonlinear focusing

Now we start the study of the transition from the linear- to the nonlinear focusing of the axisymmetric grating by increasing the amplitude of the incident plane wave. The piezoelectric transducer is excited with an amplitude in which its behavior can be considered linear in the range of frequencies from $0.5f/f_0$ to $1.5f/f_0$. In this range of frequencies we reproduce the same acoustic pattern as in the linear (small amplitude excitation) regime showing the focal spot at $f/f_0 = 1$ and at $z = F$, as shown in Fig. 5.8 (a). However, now we can clearly see that the focal spot has contributions fro the double frequency $f/f_0 = 2$, i.e., at the second harmonic of the fundamental wave. The high amplitude around the spot generated at frequency $f/f_0 = 1$ activates the harmonic generation due to the nonlinearity of water, activating the contribution from $f/f_0 = 2$ due to the high amplitudes around the focal spot.

The focal spot generated by this nonlinear effect presents a spatial acoustic profile with different properties than the focal spot of the fundamental mode. Because of the local nonlinear generation of this spot, the longitudinal profile presents smaller lobes than in the case of the spot of the fundamental frequency. Figure 5.8 (b) shows the comparison between the experimental longitudinal profile for (continuous line) first harmonic and (dashed line) its corresponding second harmonic.

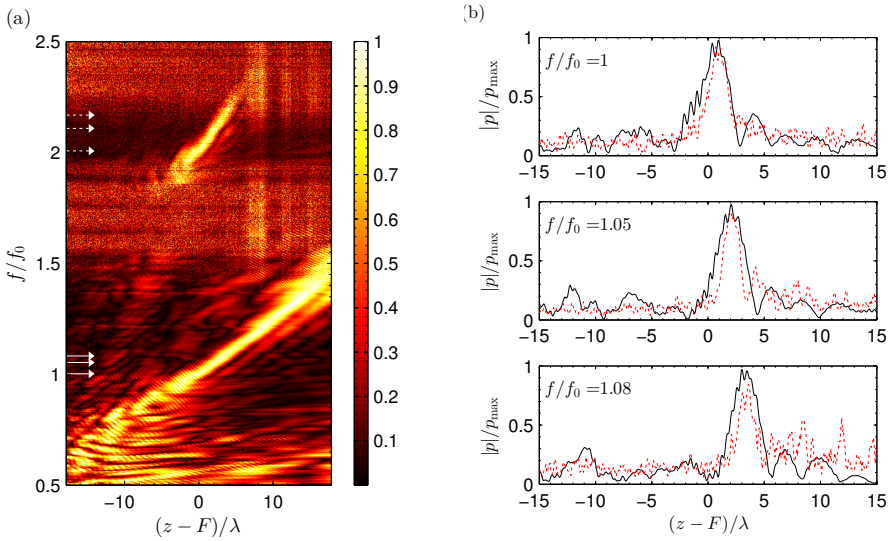


Figure 5.8: Weakly nonlinear experimental measurements of the grating. (a) On-axis field distribution as a function of the frequency. (b) On-axis field distribution for the second harmonic for three frequencies, marked by the arrows in (a). Experiments (Red dotted line) and simulation (continuous line).

5.5 High intensity regime

We explore the high amplitude regime by using nonlinear simulation methods based also in FDTD technique, as used previously in Chapter 3. The simulations assumed perfectly rigid scatters over a cylindrical axisymmetric coordinate system, where the nonlinearity is only present on the bulk of the fluid, in this case we assumed water, with parameters: $\beta = 1 + B/2A = 3.5$, density $\rho_0 = 1000$, sound speed $c_0 = 1500$.

An overview of the device focusing for increasing source amplitude is shown in Fig. 5.9. The source amplitude is expressed as the normalized quantity F/x_s, being $x_s = 1/k\varepsilon\beta$ the shock formation distance with k the wavenumber, ε the acoustic match number and β the parameter of nonlinearity. In Fig. 5.9, we show the axial peak pressure distribution, i.e. the maximum of the nonlinear waveforms, $|p|^+$, and the minimum rarefaction distribution, $|p|^-$. On the other hand, in Fig. 5.10 it is shown the lateral pressure distribution corresponding also to $|p|^+$ and $|p|^-$ for the same range of excitation amplitudes.

The main nonlinear effects in the field distribution in high intensity focused ultrasound can be observed here. The effective gain of the system, the peak value corresponding to $p_{\max}/p_0$, is extraordinary increased from the linear value of $p/p_0 = 39$ (32 dB), to $|p|^+/p_0 = 92$ (39 dB) in the case of very strong nonlinearity. Thus, as peak pressure grows locally at the focus, the focal width stretches in both axial and lateral dimensions. In addition, the relative amplitude between the peak pressure and its lateral lobes is strongly increased.

In Figure 5.11 we illustrate the pressure distribution for 4 different source

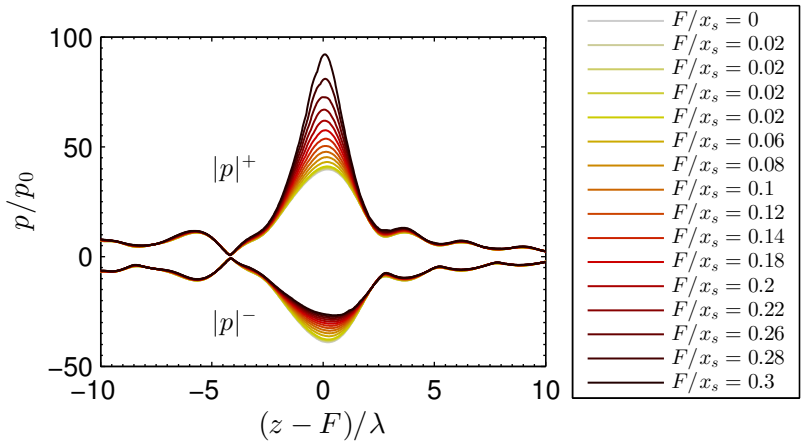


Figure 5.9: Axial simulated pressure profile for the positive envelope ($|p|^+$) and for the rarefaction minimum distribution ($|p|^-$). Different excitation amplitudes are marked as different color lines.

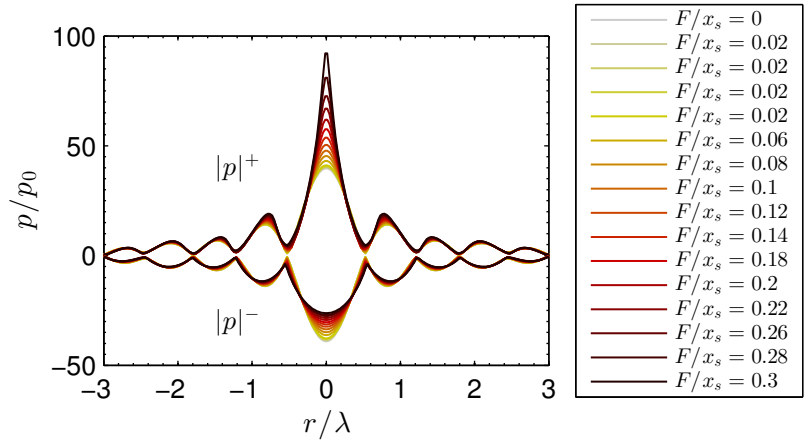


Figure 5.10: Transversal simulated pressure profile for the positive envelope ($|p|^+$) and for the rarefaction minimum distribution ($|p|^-$). Different excitation amplitudes are marked as different color lines.

amplitudes, being $F/x_s = 0.02, 0.16, 0.260.3$ from low to high amplitude. The above described effects can be observed. The axial field distribution corresponding to these amplitudes can be observed in Fig. 5.12, where the amplitude of the first and second harmonic is extracted. It can be seen that the amplitude of the first harmonic is slightly reduced for increasing amplitudes and the second harmonic field grows locally at the focal spot.

The locally nonlinear generation of the higher harmonics contributes to modify the waveform, shown in the corresponding subplots of Fig. 5.12. Here, the characteristic shape of nonlinear focused waveforms can be observed, reaching a peak pressure of $|p|^+ = 126$ MPa and a rarefaction pressures of $|p|^+ = -36$ MPa. These peak pressures are of the order of those used in medical therapy applications for thermal ablation, with the rarefaction pressure close to the cavitation threshold of the water at room hydrodynamic pressure and temperature[1] (Caupin et al., 2006).

[1]Note the cavitation threshold strongly depends of the dissolved oxygen content and bubbles in general of the water.

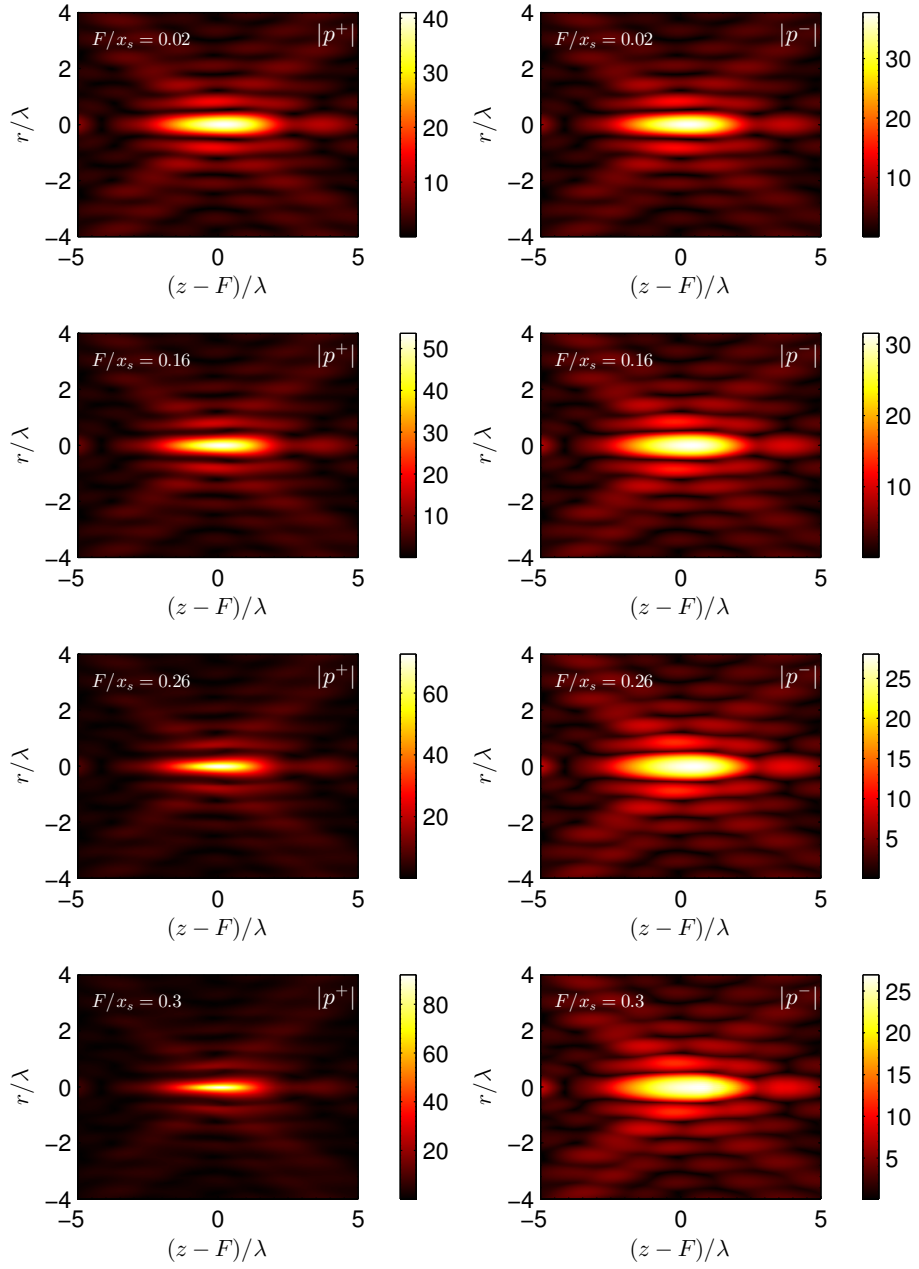


Figure 5.11: Field distribution for increasing amplitude excitation. (Left column) pressure profile for the positive envelope ($|p|^+$) and (right column) for the rarefaction minimum distribution ($|p|^-$).

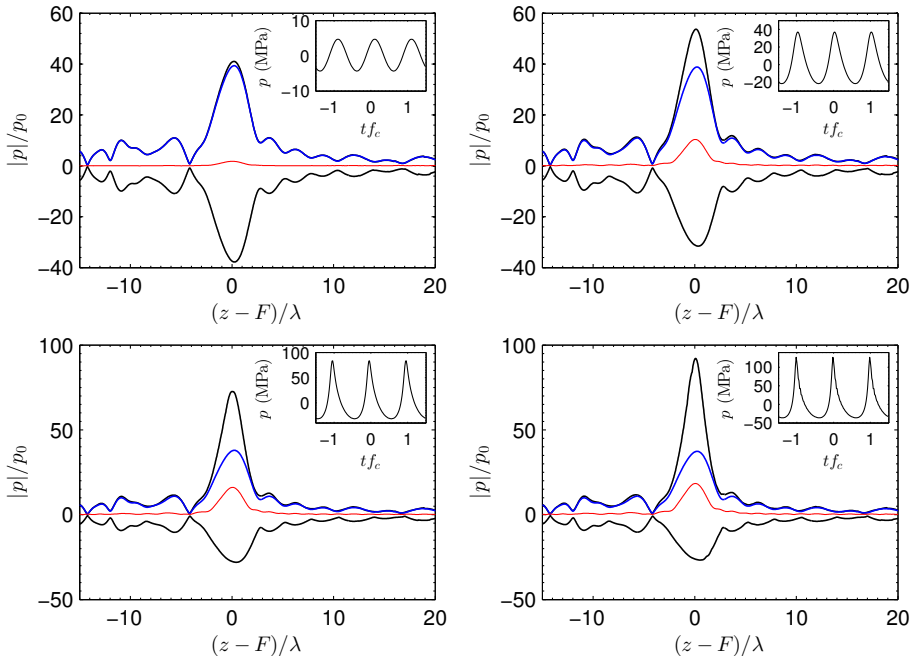


Figure 5.12: Axial field distribution for four increasing amplitudes, being $F/x_s = 0.02, 0.16, 0.260.3$ from low to high amplitude. (Black lines) full envelopes $|p|^+$ and $|p|^-$, (blue) fundamental harmonic component and (red) second harmonic field distribution. The inset shows the corresponding waveforms measured at the focal in physical units.

Finally, from all these the simulation data, the nonlinear dependence of the focusing parameters of the grating is calculated and presented in Fig. 5.13. In first place, the nonlinear gain of the system is shown in Fig. 5.13 (a), where it is plotted the gain for the full peak amplitudes ($|p|^+/p_0$ and $|p|^-/p_0$), and also the corresponding gain for the first, second and third harmonics. It can be seen that the nonlinear effects dramatically increases the peak pressure gain due to the strong asymmetry of the waveforms. In the same way, the gain for the rarefaction pressure decreases with excitation amplitude also due to the asymmetry of the nonlinear distortion at focus (see insets in Fig. 5.12). The gain for the first harmonic is almost constant, around 40 dB, but it slightly reduces for increasing amplitudes as long energy is transferred to higher harmonics. Finally, the gain for second and higher harmonics increases. In the case of second harmonic it varies from 0 to about the half of the linear gain of the system.

There exist also a nonlinear focal shift in the location of the peak pressure, shown in Fig. 5.13 (b). Thus, as the source amplitude is increased the location of the peak pressure is displaced in the axial direction beyond the linear focal position, a self-defocusing effect is observed. On the other hand, for the case of the rarefaction pressure it appears a nonlinear self-focusing effect, i.e. the focal

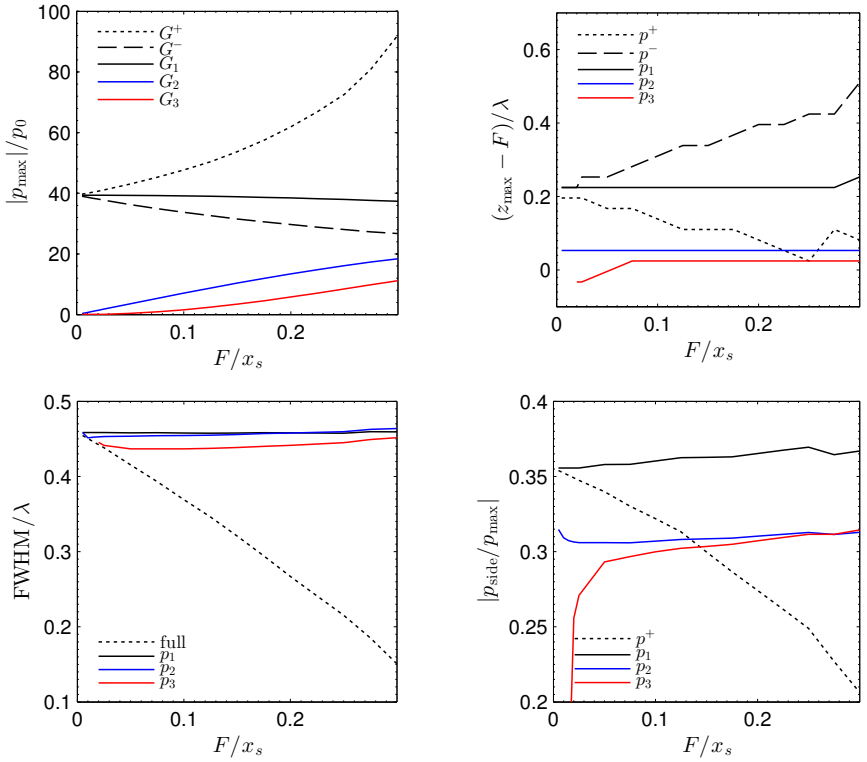


Figure 5.13: Focal characterization in the nonlinear regime. (Up left) Effective gain obtained as $|p_{max}|/p_0$ as a function of the normalized excitation amplitude. (Up right) Location of the peak pressure. (Bottom left) Intensity Full Width at Half Maximum (FWHM), also normalized by the harmonic index. (Bottom right) Side lobe amplitude as a function of the excitation amplitude.

displaces towards the source. Both effects can be related to nonlinear self-refraction of the beam in the focal spot (Camarena et al., 2013a). However, due to the low focal size of this strongly focused device (Camarena et al., 2010) these effects are minor and the total displacements are not longer that $\lambda/4$.

We have analyzed the FWHM of the several harmonics as the amplitude of the incident wave in increased. Figure 5.13 (c) shows the dependence of FWHM on the amplitude of the incident wave, measured again in terms of the shock distance normalized to the focal position in the linear regime, F. FWHM is constant for both the fundamental and the second harmonic focal spots, note here that the second harmonic focal size is effectively half of the size of the fundamental wave, but we show the value normalized to its wavelength. It is worth noting here, that as the nonlinearity of the medium is activated, the focal spot considering all the components, decreases dramatically its FWHM because of the strong asymmetry of the waveforms only at the focal spot.

Finally, we can compare the different transversal profiles and observe the reduction of the side lobes of the second-and-higher harmonic profiles. The numerical results show the highly reduced lobes around the focal spot both in the radial and in the longitudinal directions. This effect is caused by the locally generation of the field only at the focal spot, where in the other hand, the nonlinear (local) harmonic generation at the lateral lobes is reduced due to its low amplitude. It is worth noting here that the reduction does not strongly depends on the excitation amplitude: very weak nonlinear effects are enough to provide second harmonic side-lobe reduction.

5.6 Conclusions

We have presented a characterization of the focusing properties of an axisymmetric grating constructed by toroidal scatters. The design is equivalent to a binary Fresnel lens of infinitesimally thicker slits. We demonstrated experimentally and numerically that the device presents a very narrow focal spot, that is between the sub-diffraction and the sub-wavelength limits. As common from other Fresnel-like lenses and also in Bessel beams, the narrow focal is accompanied by high amplitude side lobes. On the other hand, the confined focal provides strong energy concentration over a small volume. Thus, nonlinear effects can be mainly activated locally at the focal spot, and second harmonic is generated mainly there. In this way, the field of the second harmonic maintain the excellent beam-width of the Fresnel lens, while its side-lobes are strongly reduced. The proposed lens in the weakly nonlinear regime is suitable for second harmonic imaging techniques: the excellent beam spatial resolution of the second harmonic (normalized to the wavelength) is maintained, while the side-lobe amplitude, responsible of signal-to-noise ratio, is reduced.

Another important feature is related to the energy concentration of the system. In the proposed system, an amplification of the incident field up to 30 dB has been observed numerically and experimentally. A parametric study shows that amplification values up to 35 dB can be also obtained if the number of rings, i.e. the aperture, are increased to $M = 50$.

Finally, it is worth noting here that the device is designed for single frequency operation. The chromatic aberration for frequencies around the design frequency is not strong: for a relatively broad bandwidth, around one octave, the main observed effect in simulations and experiments is a focal shift. The focal spot shifts in the axial direction and the displacement can be estimated analytically. For the presented device a focal displacement of about 30 wavelengths has been observed in the frequency range studied. The gain also is modified by the chromatic aberration, but notice that these variations can be compensated by signal processing. In this way, the focal aberration provides a way to actively change the axial location of the sharp focus if the passive device is excited by a frequency modulated signal.

Thus, it can provide a cheap alternative to ultrasound imaging techniques that requires a fast intense moving focal, as in Supersonic Shear Imaging.

References

Averkiou, Michalakis A, David N Roundhill, and JE Powers (1997). "A new imaging technique based on the nonlinear properties of tissues". In: *Ultrasonics Symposium, 1997. Proceedings., 1997 IEEE*. Vol. 2. IEEE, pp. 1561–1566.

Bailey, MR, VA Khokhlova, OA Sapozhnikov, SG Kargl, and LA Crum (2003). "Physical mechanisms of the therapeutic effect of ultrasound (a review)". In: *Acoustical Physics* 49.4, pp. 369–388.

Bercoff, Jérémy, Mickaël Tanter, and Mathias Fink (2004). "Supersonic shear imaging: a new technique for soft tissue elasticity mapping". In: *Ultrasonics, Ferroelectrics, and Frequency Control, IEEE Transactions on* 51.4, pp. 396–409.

Botteldooren, Dick (1995). "Finite-difference time-domain simulation of low-frequency room acoustic problems". In: *The Journal of the Acoustical Society of America* 98.6, pp. 3302–3308.

Camarena, Francisco, Yuri Makov, Víctor Sánchez-Morcillo, Silvia Adrián, and Noé Jiménez (2010). "Nonlinear focal shift in medium Fresnel-number focused acoustic beams". In: *Ultrasonics Symposium (IUS), 2010 IEEE*. IEEE, pp. 1845–1848.

Camarena, Francisco, Silvia Adrian-Martinez, Noe Jimenez, and Victor Sanchez-Morcillo (2013a). "Nonlinear focal shift beyond the geometrical focus in moderately focused acoustic beams". In: *The Journal of the Acoustical Society of America* 134, pp. 1463–1472.

Canney, Michael S, Michael R Bailey, Lawrence A Crum, Vera A Khokhlova, and Oleg A Sapozhnikov (2008). "Acoustic characterization of high intensity focused ultrasound fields: A combined measurement and modeling approach". In: *The Journal of the Acoustical Society of America* 124.4, pp. 2406–2420.

Caupin, Frédéric and Eric Herbert (2006). "Cavitation in water: a review". In: *Comptes Rendus Physique* 7.9, pp. 1000–1017.

Choi, James J, Mathieu Pernot, Scott A Small, and Elisa E Konofagou (2007). "Noninvasive, transcranial and localized opening of the blood-brain barrier using focused ultrasound in mice". In: *Ultrasound in medicine & biology* 33.1, pp. 95–104.

Clement, G., H. Nomura, and T. Kamakura (2015). "Ultrasound field measurement using a binary lens". In: *Ultrasonics, Ferroelectrics, and Frequency Control, IEEE Transactions on* 62.2, pp. 350–359.

Cunningham, Kevin B and Mark F Hamilton (2000b). "Bessel beams of finite amplitude in absorbing fluids". In: *The Journal of the Acoustical Society of America* 108.2, pp. 519–525.

Ding, Desheng and Zuhong Lu (1996). "The second harmonic component in the Bessel beam". In: *Applied physics letters* 68.5, pp. 608–610.

Ding, Desheng and L Jian-yu (2000b). "Higher-order harmonics of limited diffraction Bessel beams". In: *The Journal of the Acoustical Society of America* 107, pp. 1212–1214.

Duck, Francis A (2002). "Nonlinear acoustics in diagnostic ultrasound". In: *Ultrasound in medicine & biology* 28.1, pp. 1–18.

Farnow, SA and BA Auld (1974). "Acoustic Fresnel zone plate transducers". In: *Applied Physics Letters* 25.12, pp. 681–682.

Holm, Sverre and Fabrice Prieur (2010). "Low sidelobe limited diffraction beams in the nonlinear regime". In: *The Journal of the Acoustical Society of America* 128.3, pp. 1015–1020.

Hsu, DK, FJ Margetan, and DO Thompson (1989b). "Bessel beam ultrasonic transducer: Fabrication method and experimental results". In: *Applied physics letters* 55.20, pp. 2066–2068.

Jimenez, Noe, Vicente Romero-García, R Picó, A Cebrecos, Víctor José Sánchez-Morcillo, LM Garcia-Raffi, Juan Vicente Sánchez-Pérez, and K Staliunas (2014). "Acoustic Bessel-like beam formation by an axisymmetric grating". In: *EPL (Europhysics Letters)* 106.2, p. 24005.

Konofagou, Elisa E and Kullervo Hynynen (2003). "Localized harmonic motion imaging: theory, simulations and experiments". In: *Ultrasound in medicine & biology* 29.10, pp. 1405–1413.

Lu, J.-y. and J.F. Greenleaf (1990b). "Ultrasonic nondiffracting transducer for medical imaging". In: *Ultrasonics, Ferroelectrics, and Frequency Control, IEEE Transactions on* 37.5, pp. 438–447.

Molerón, M., A. Leonard, and C. Daraio (2014). "Solitary waves in a chain of repelling magnets". In: *J. Appl. Phys.* 115.18, p. 184901.

Nguyen, Man Minh, Junseob Shin, and Jesse Yen (2014). "Harmonic Imaging with Fresnel Beamforming in the Presence of Phase Aberration". In: *Ultrasound in medicine & biology* 40.10, pp. 2488–2498.

Nightingale, Kathryn, Mary Scott Soo, Roger Nightingale, and Gregg Trahey (2002). "Acoustic radiation force impulse imaging: in vivo demonstration of clinical feasibility". In: *Ultrasound in medicine & biology* 28.2, pp. 227–235.

Sarvazyan, Armen P, Oleg V Rudenko, Scott D Swanson, J Brian Fowlkes, and Stanislav Y Emelianov (1998). "Shear wave elasticity imaging: a new ultrasonic technology of medical diagnostics". In: *Ultrasound in medicine & biology* 24.9, pp. 1419–1435.

Schindel, DW, AG Bashford, and DA Hutchins (1997). "Focussing of ultrasonic waves in air using a micromachined Fresnel zone-plate". In: *Ultrasonics* 35.4, pp. 275–285.

Sleva, Michael Z, William D Hunt, and Ronald D Briggs (1994). "Focusing performance of epoxy- and air-backed polyvinylidene fluoride Fresnel zone plates". In: *The Journal of the Acoustical Society of America* 96.3, pp. 1627–1633.

Wang, Hui, Da Xing, and Liangzhong Xiang (2008). "Photoacoustic imaging using an ultrasonic Fresnel zone plate transducer". In: *Journal of Physics D: Applied Physics* 41.9, p. 095111.

Publications

The contents of this Chapter have been presented in the following publications:

Journal papers

- **Jiménez, N.**; Romero-García, V.; Picó, R.; Cebrecos, A.; Sánchez-Morcillo, V.; García-Raffi, L.; and Staliunas, K. "Transition from linear- to nonlinear-focusing regime of ultrasonic waves produced by an axisymmetric diffraction grating" *In preparation* (2015)